Journal of Applied Fluid Mechanics, Vol. 17, No. 4, pp. 770-784, 2024.
Available online at www.jafmonline.net, ISSN 1735-3572, EISSN 1735-3645.
https://doi.org/10.47176/jafm.17.4.2274

Flow Field Analysis of Francis Turbine Draft Tube using POD at Design and Part Load Operating Conditions

S. Kumar[1†], M. J. Cervantes[2] and B. K Gandhi[1]

[1] *Department of Mechanical and Industrial Engineering, Indian Institute of Technology, Roorkee, Uttarakhand, 247667, India*
[2]*Division of Fluid and Experimental Mechanics, Department of Engineering Sciences and Mathematics, Lulea University of Technology, 97187, Sweden*

†*Corresponding Author Email: skumar6@me.iitr.ac.in*

ABSTRACT

The hydraulic turbines, especially Francis turbines, frequently run at part load (PL) conditions to meet the dynamic energy needs. The flow field at the runner exit changes significantly with a change in the operating point. At PL, flow instabilities such as the Rotating Vortex Rope (RVR) form in the draft tube of the Francis turbine. The present paper compares the features of the velocity and vorticity field of the Francis turbine draft tube at the best efficiency point (BEP) and PL operations using the Proper Orthogonal Decomposition (POD) of the 2D-PIV data. The POD analysis decomposes the flow field into coherent and incoherent structures describing the spatiotemporal behavior of the flow field. A visual representation of the coherent structures and the turbulent length scales in the flow field is extracted and analyzed for BEP and PL, respectively. The study highlights the salient features of the draft tube flow field, which differentiate the BEP and PL operation. The fast Fourier transform of the temporal coefficients confirms the presence of RVR frequency (0.29 times the runner frequency) at PL. The phase portraits of different modes elucidate the relationship between different harmonics of the RVR frequency at PL.

Article History

Received August 30, 2023
Revised November 8, 2023
Accepted November 17, 2023
Available online January 30, 2024

Keywords:

POD
Part load
Vortex rope
Dissipation
Francis Turbine

1 Introduction

The Francis turbines are the most widely used hydraulic turbines for generating electric power. Apart from producing electricity, these turbines are being increasingly used to regulate the power grid by varying their power output. These frequent changes in power output concern Francis turbines designed for a single operating point known as the BEP. The flow field at the runner exit changes significantly with a change in the operating point.

At off-design conditions, the flow field inside the draft tube is non-uniform because of the swirling or tangential velocity component. It leads to the onset of flow instabilities in the draft tube, which affect the performance of the hydraulic turbine (Wang et al., 2022). The nature and characteristics of flow instabilities mainly depend on the swirl number, which is the ratio of the tangential to the axial component of velocity (Sarpkaya, 1971). The increase in tangential momentum of the flow at off-design operations increases the swirl at the exit of the runner (Kumar et al., 2021a).

At PL operation, the velocity distribution in the draft tube of the Francis turbine depends on both the swirl strength and adverse pressure gradient (APG) due to the diverging flow passage. The APG and the swirling flow induce a radial pressure gradient, leading to flow deceleration and a stagnant flow region at the draft tube center. After a particular condition, the main axial flow's kinetic energy (KE) cannot overcome the APG in the draft tube cone (Goyal et al., 2023). This results in flow reversal at the core, leading to a helical vortical structure known as the RVR. The RVR precesses eccentrically to the draft tube axis (Litvinov et al., 2022), and the direction of rotation is the same as that of the runner. The RVR leads to low-frequency pressure pulsations, pulsative pressure recovery, power swings, noise, and vibrations at the part load operation (Khozaei et al., 2022; Salehi & Nilsson, 2022). The precessing of the RVR combined with centrifugal, inertial, and viscous forces also generate secondary flows (like Dean Vortices) in the draft tube (Shahzer et al., 2022). These secondary flows hinder the conversion of the KE into pressure energy, reducing the draft tube efficiency.

Nomenclature

APG	Adverse Pressure Gradint	V_i	velocity vector
BEP	Best Efficiency Point	f	vortex rope frequency
G	auto covariance matrix	f_n	runner rotational frequency
GVO	Guide Vane Opening	ρ	density
HL	High Load	λ	eigen value
KE	Kinetic Energy	v_a	viscosity of fluid
N	number of snapshots	ε	dissipation
PIV	Particle Image Velocimetry	τ_{ij}	symmetric tensor,
POD	Proper Orthogonal Decomposition	$\overrightarrow{\xi^m}$	spatial mode
PL	Part Load	α_i^m	temporal coefficient
RVR	Rotating Vortex Rope	$(\wedge)$	Taylor macro
S	local fluctuating strain rate tensor	(π)	Taylor micro
TKE	Turbulent Kinetic Energy	φ	phase angle

Due to the adverse effects of RVR, the flow characteristics leading to its formation have been an active field of investigation. Researchers have put various theories to explain the phenomenon of RVR formation. However, the structure of RVR and its breakdown into the flow field is still not completely understood. The authors try to deduce the structure of RVR and the unstable flow field in the draft tube through POD. The POD method effectively separates the turbulent dominant flow structures (coherent structures) from the main flow. It works on the eigenvalue problem, relying on the energy maximization principle (Podvin & Fraigneau, 2017). The snapshot POD method can extract the physical information of the flow structures for a set of POD modes, which can then be arranged in decreasing order of energy contribution (Kostas et al., 2005; Tutkun & George, 2017). Therefore, the coherent structures or modes with high energies are searched in the turbulent flow field by POD and are likely to be characterized by POD functions (Doulgerakis, 2010; Liné et al., 2013; Liné, 2016).

In hydro turbines, POD was first introduced by Pavel Rudolf (Rudolf & Jízdný, 2011) in the conical draft tube. The input data for snapshots POD was obtained from numerical simulations. Pavel Rudolf (Rudolf & Jízdný, 2011) reconstructed the large coherent structure known as RVR through pressure isosurfaces. Rudolf (Rudolf & Štefan, 2012; Rudolf et al., 2019) and Stefan (Stefan & Rudolf, 2015) applied POD on the static pressure field and reconstructed the vortex rope through static pressure isosurfaces to reconstruct only the RVR. Rudolf et al. (2013) and Rudolf and Štefan (2014) also numerically analyzed the axial and radial components of the velocity of the conical part of a swirl generator at PL condition using Reynolds Averaged Navier-Stokes (RANS) model. Further, Stefan (2017) applied snapshot POD on unsteady 3D numerical data of velocity and pressure field to investigate the effectiveness of water jet injection in mitigating RVR. These studies tried only to reconstruct the RVR through isosurfaces and did not completely analyze the structure of vortex breakdown and flow field in the draft tube.

The present work reports a detailed qualitative comparison of the flow field in the draft tube of a Francis turbine at BEP and 70% PL operating conditions. The snapshot POD method is employed on the 2D PIV data to investigate the turbulent flow field. The main objective is identifying the coherent structures forming at BEP and PL operating conditions. The differentiation between BEP and PL will highlight the aspects that lead to the development of flow instabilities and RVR in the draft tube. The modal decomposition tracks the formation of RVR. Understanding the flow field is important for devising suitable methodologies for RVR mitigation.

The PIV data is decomposed into different modes relevant to the flow field. The quantities like generation and dissipation of total kinetic energy (TKE) and different turbulent length scales present in the flow field at PL and BEP operations are estimated. The present study also gives an insight into the fraction of energy dissipation due to secondary flow structures developed during RVR formation. Coherent modes of the POD represent these structures and elucidate the aspects of the formation mechanism of the RVR. The analytical and numerical studies in the literature validate certain aspects of the coherent structure.

The paper is divided into six sections. The second section presents the methodology and validation of the POD code. In the third section, the KE of POD modes is presented. The fourth section presents the dissipation of KE of different POD modes at BEP and PL operating points. The coherent structures obtained after the flow field decomposition are presented in this section. The characteristic turbulent length scales for the two operating points are estimated in the fifth section. The last section presents the phase portraits of different modes.

2 METHODOLOGY AND VALIDATION

Proper orthogonal decomposition (POD) has been extensively used to investigate turbulent flow fields (Lumley, 1967; Lumley & Meyer, 1981; Sirovich, 1987a). It provides detailed and useful information about the dominant organized flow patterns in the flow field. Lumley (Lumley, 1967; Lumley & Meyer, 1981) reported the classical idea of an optimal orthogonal projection, identifying large-scale energy-carrying deterministic modes in the turbulent flow field. POD is simply a linear procedure that works on the spectral theory of compact operator and Hermitian operator (Berkooz et al., 1993). Sirovich (Sirovich, 1987a, b, c) later developed an

Algorithm: Proper Orthogonal Decomposition (POD)

Required: A sequence of *N* snapshots [S_1, S_2, S_3,……..,S_n] sampled equi-spaced in time with Δt.

Output: Eigen value spectrum (λ_G) and associated POD modes " m_j" with $j = 1,2,3,\ldots\ldots, n$

- *The instantaneous velocity component data has l rows and c columns arranged in a matrix. A matrix H having 2lc rows and N columns*

$$H=\begin{pmatrix} u^1_{(x_1,y_1)} & u^2_{(x_1,y_1)}\cdots & u^N_{(x_1,y_1)} \\ u^1_{(x_2,y_1)} & u^2_{(x_2,y_1)}\cdots & u^N_{(x_2,y_1)} \\ \vdots & \ddots & \vdots \\ u^1_{(x_c,y_l)} & u^2_{(x_c,y_l)}\cdots & u^N_{(x_c,y_l)} \\ v^1_{(x_1,y_1)} & v^2_{(x_1,y_1)}\cdots & v^N_{(x_1,y_1)} \\ v^1_{(x_2,y_1)} & v^2_{(x_2,y_1)}\cdots & v^N_{(x_2,y_1)} \\ \vdots & \ddots & \vdots \\ v^1_{(x_c,y_l)} & v^2_{(x_c,y_l)}\cdots & v^N_{(x_c,y_l)} \end{pmatrix}$$

- *An auto-covariance tensor matrix (G) can be derived by*

$$G=\frac{1}{N}\left(H.H^T\right)$$

- *The eigenvalue problem is then solved for this auto-covariance matrix G is given by*

$$GA^i=\lambda^i A^i$$

- *Ranked in decreasing order according to the size of the eigenvalue is given by*

$$\lambda^1>\lambda^2>\cdots\cdots\cdots>\lambda^N=0$$

- *The snapshot, which represents the instantaneous velocity flow field, can be extended to a series of POD modes. When these velocity fields are projected on the m^th Eigen function value* $\overrightarrow{\xi^m}$ *, the POD coefficients* α_i^m *are obtained by*

$$\alpha_i^m=\overrightarrow{V_i}.\overrightarrow{\xi^m}$$

- *The m^th velocity vector corresponds to m^th decomposition and is given below. The velocity field represented by a snapshot can be reconstructed by*

$$\overrightarrow{V_i}(x,y)=\sum_{i=1}^{N}\overrightarrow{V_i^m}(x,y)=\sum_{i=1}^{N}\alpha_i^m\overrightarrow{\xi^m}(x,y)$$

Fig. 1 POD Algorithm

effective algorithm called the snapshot or snapshot POD method. The method could yield the same deterministic spatial modes from the temporal correlation matrix as given by Lumley's POD method. The algorithm for snapshot POD is described in Fig. 1 (Sirovich, 1987a; Berkooz et al., 1993; Kumar et al., 2019; Kumar et al., 2021b).

In the present study, POD is applied to the instantaneous velocity field to find the mean properties and decomposition of the flow field. The mean flow mode is the first mode obtained from the instantaneous velocity field. Mode 2 to mode 250 can also be obtained from the orthogonal decomposition of the fluctuating velocity field. The time-dependent snapshots are decomposed into the spatial modes $\overrightarrow{\xi^m}$, and temporal coefficients as described in the algorithm in Fig.1.

The PIV measurement data for the 2D plane, as shown in Fig. 2, was available from the measurements performed by Goyal et al. (Goyal, 2017; Goyal et al., 2017a). Goyal et al. (2017a, b, c, 2018) performed 2D PIV measurements on the central plane in the draft tube cone of the model Francis-99 turbine. The PIV measurements (a mesh grid of 83x126 data points) were performed at a sampling frequency of 40 Hz at different operating points. Two operating points BEP and 70% PL, were considered for the investigation. The Reynolds number at the draft tube inlet was 7.1 x 10^5 and 5.1 x 10^5 at BEP and PL,

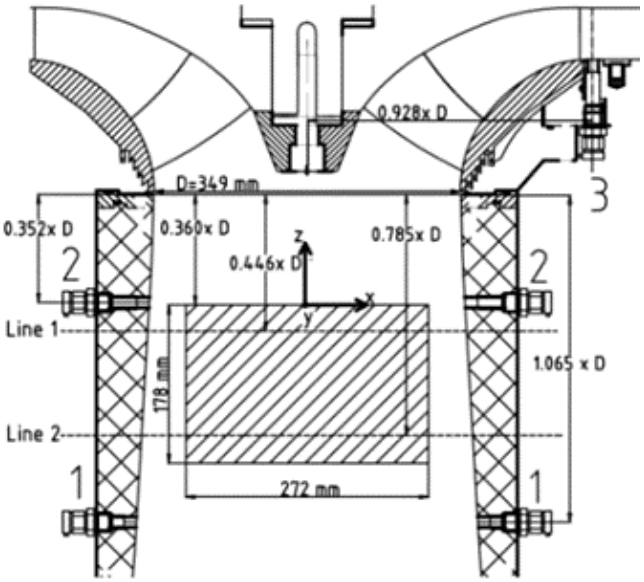

Fig. 2 PIV measurement plane of Francis-99 test case (Goyal, 2017)

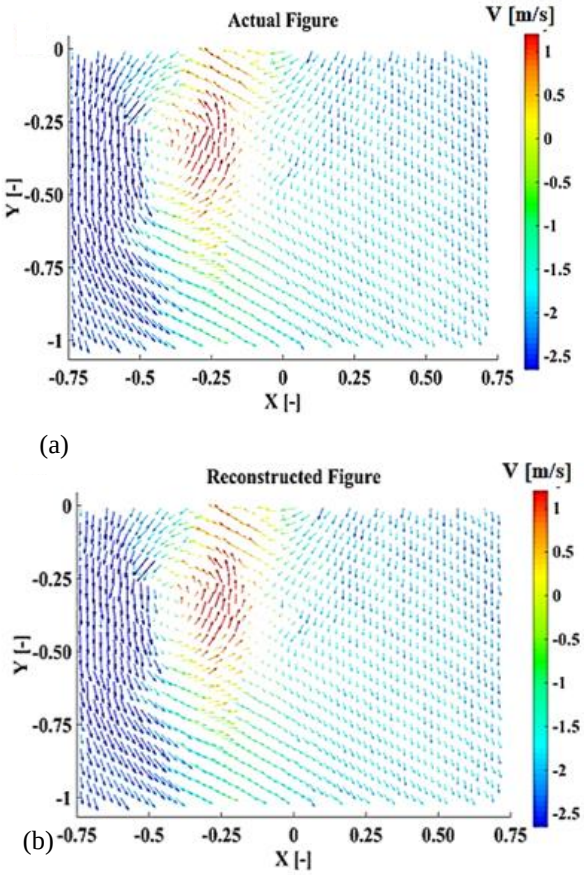

Fig. 3 Vector plot of a random actual image; (b) Vector plot of reconstructed image from all 250 modes (Kumar et al., 2021b).

respectively. The spatial resolution of the PIV measurement was 2.1 mm, and the data was recorded for60 seconds. Goyal (Goyal, 2017; Goyal et al., 2017a) showed that 120 images were sufficient to obtain results qualitatively identical to those based on 2400 snapshots.

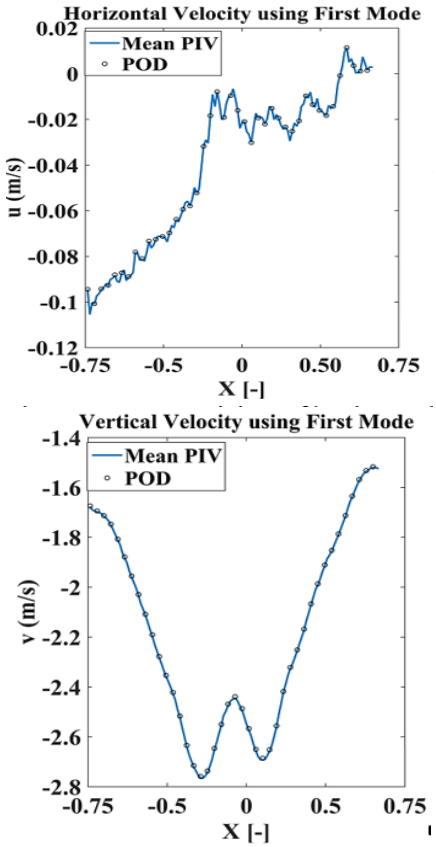

Fig. 4 Comparision of horizontal and vertical velocities obtain from PIV and snapshot POD.

The POD methodology in present work is applied on 250 PIV snapshots for the two operating conditions.

To validate the code, a random instantaneous snapshot (Fig. 3(a)) of the velocity field obtained from the PIV data at PL operating condition is reconstructed using all 250 POD modes, as shown in Fig. 3(b). The x-coordinate has been normalized to the draft tube inlet radius. The color scheme of vectors in the vector plot is for axial velocity. Since the main flow is in the negative Y direction, the positive velocities show the reverse flow in the draft tube. The reconstructed velocity field is the same as the original or actual snapshot. A horizontal line in the plane's center (Y = -0.5 in Fig. 3(b)) was created to validate both horizontal and vertical velocity data. The mean axial (vertical) and radial (horizontal) flow velocities of the first POD mode and mean flow velocities obtained through experiments (PIV) at BEP match perfectly on this line, as shown in Fig. 4. Thus, the algorithm applied is correct and can be used for further analysis.

The energy of each mode is calculated by normalizing the eigenvalue of each mode obtained in step 4 of the algorithm. The number of eigenvalues equals the number of snapshots used for decomposition. The normalized energies of the first 10 modes for BEP and PL are shown in Fig. 5. The difference between the two plots can be seen. At BEP, mode 1 has almost all the energy, around 99.21%, while the other modes have energy lower

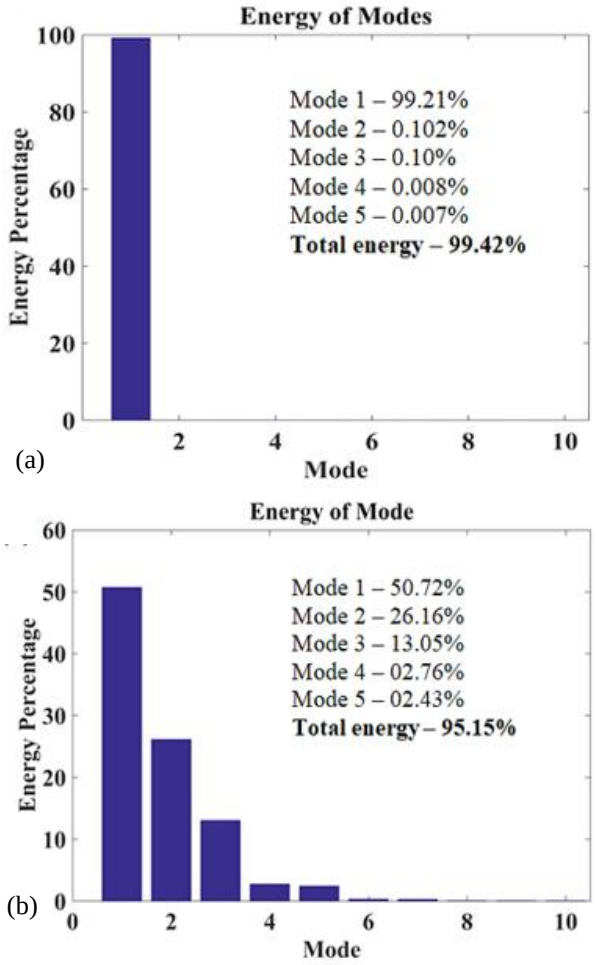

Fig. 5 Comparison of energy of first ten modes at (a)BEP; (b) PL (Kumar et al., 2021b)

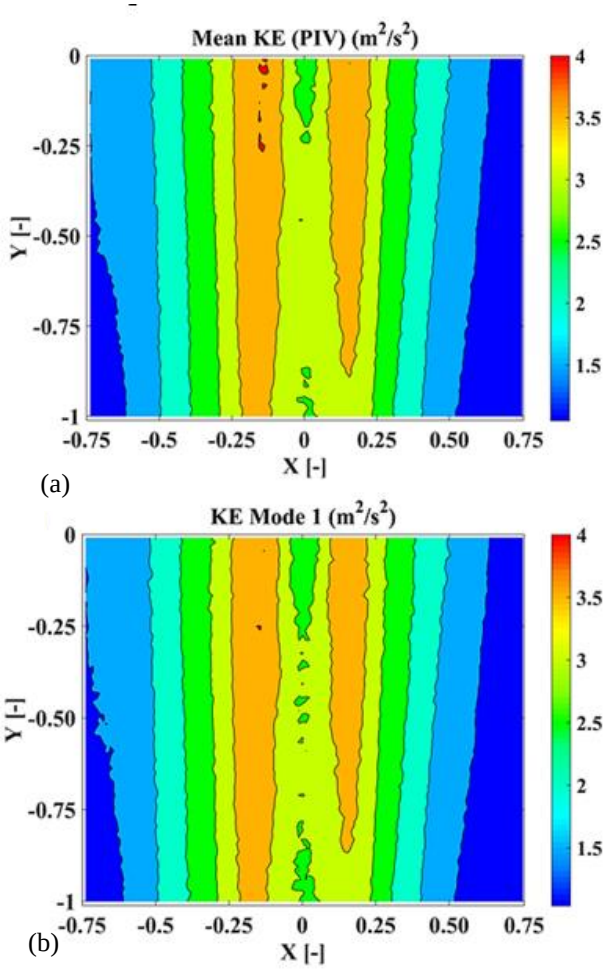

Fig. 6 (a) Mean KE obtained from PIV; (b) KE of mode 1

than 0.15%. This indicates that the flow field at BEP remains steady with time, and the velocity field is almost identical to the mean velocity field at all times. Thus, no flow instabilities are present at the BEP condition. As the instabilities are generated at PL, the energy of the first mode decreases. Unlike BEP, the first mode at PL has slightly more than 50% of the total energy and corresponds to the mean flow. Mode 2 contains about 26% of the total energy, and mode 3 has around half the energy of the 2nd mode. Mode 4 and mode 5 have almost the same energy. Mode 6 and mode 7 have energies in the range of 0.03%. The contribution of modes 1 to 5 is more than 95.5% of the total energy, which is still less than the first mode's energy at BEP.

3 RESULTS AND DISCUSSIONS

3.1 Kinetic Energy of Pod Modes

The kinetic energy (KE) is estimated from 2D PIV measurements using equation 1. Only two instantaneous velocity components were available due to measurement limitations. The KE in equation (1) is equivalent to half of the sum of the squares of these two components.

$$K(x,y)=\frac{1}{2}\sum_{i=1}^{N}\lambda^{m}\overrightarrow{\xi_i^m}(x,y)\bullet\overrightarrow{\xi^m}(x,y) \qquad (1)$$

Figure 6 presents a comparison of the mean flow KE obtained experimentally (Fig. 5(a)) and first mode KE (Fig. 6(b)) at BEP condition. The KE of the mean flow almost resembles the KE of the first mode, and it can be concluded that the first mode of BEP represents the mean flow (see Fig. 6 (a-b).

The coherent structures at both BEP and PL operating conditions were compared. The streamlines and vorticity of the mean mode 1 for the two operating conditions are presented in Fig. 7(a) and 7(b), respectively.

From Fig. 7(a), it is clear that the flow from the runner exit is mainly axial and free from any disturbance at BEP. The experimental observations also show that the azimuthal or tangential velocity component (V_t) is very small, so there is no swirling effect. The vorticity contour at the BEP condition is also shown in Fig. 7(a), and it can be observed that the vortical structures are present in the flow field for energy dissipation. The central region in BEP condition has the maximum and the minimum vorticity. Blue represents the minimum vorticity magnitude, while yellow represents the maximum vorticity magnitude region. At PL operating conditions, the V_t component is in the direction of the runner rotation (Kumar et al., 2021a). Therefore, at PL, the mean flow is inclined toward runner rotation. The axial velocity direction in the flow is disturbed, and the flow shows swirling effects, as shown in Fig 7(b). The vorticity

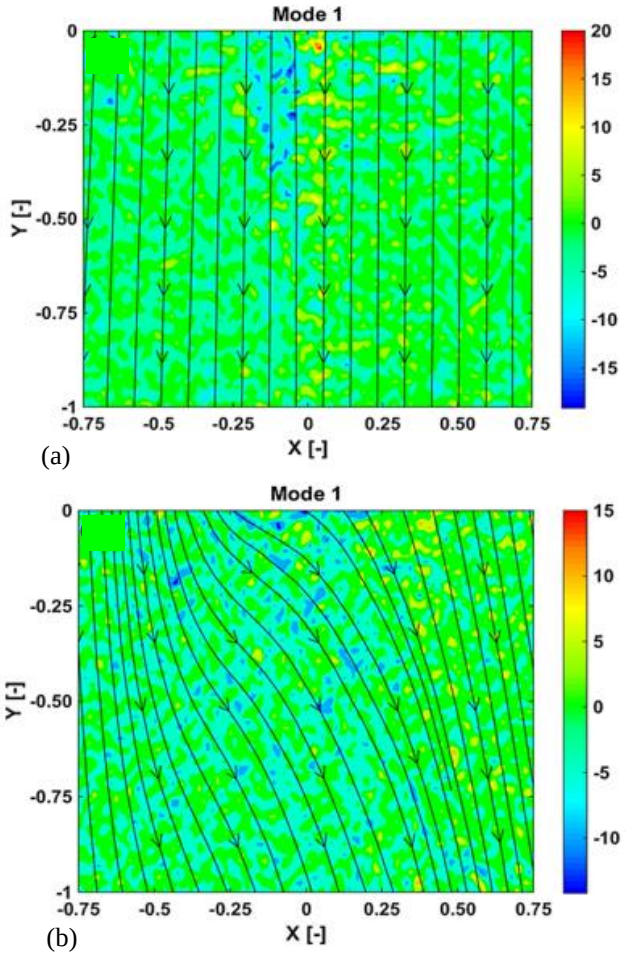

Fig. 7 (a) Vorticity contour with streamlines of mode 1 at BEP; (b) Vorticity contour with streamlines of mode 1 at PL

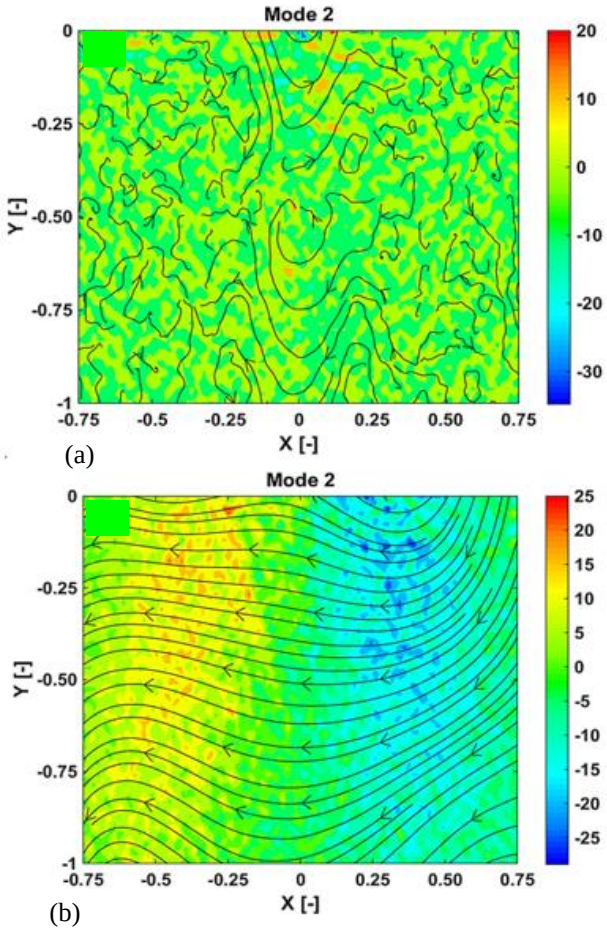

Fig. 8 (a) Vorticity contour with streamlines of mode 2 at BEP; (b) Vorticity contour with streamlines of mode 2 at PL

contour in Fig. 7(b) is dispersed in the region where the fluid is in a curved path. The vorticity is primarily negative and tries to spin the fluid clockwise.

A further study of the flow pattern indicates that modes 2 to 8 for PL and modes 2 to 4 at BEP represent coherent structures. The coherent structures are attributed to the instability of the shear layer in the flow field, such as the Kelvin-Helmholtz instability. The streamlines of mode 2 for BEP and PL operations are shown in Fig. 7. The energy contribution of mode 2 is 0.10% and 26.16% at BEP and PL, respectively. At PL, the energy contribution of mode 2 is around half that of mode 1. Figure 8(a) shows a rotating core at the draft tube center at BEP operating condition, possibly due to the runner cone profile. It is also observed that the upper part of the core rotates in the runner's direction. The lower part rotates in the opposite direction due to the vortex core's rolling. The streamlines show (Fig. 8a) some U-type patterns near the draft tube center axis. The vorticity contours show a localized mix effect at the center. Overall, vorticity in the central region has the same value. It may be attributed to a small KE of the fluid and negligible residual swirl or the wake of the runner cone.

The flow direction at PL seems opposite to the runner rotation, as shown in Fig. 8(b). It may occur because, near the RVR, the angular momentum is less in the stagnation region. The flow reversal and fluid entering the vortex core generate angular momentum and push the main flow toward the draft tube wall. It may be a counterbalance of the flow field against the swirl. It may also be a slow-moving sweeping motion parallel to the draft tube surface induced by the co-rotating and counter-flowing large eddy structure called RVR. It can also be better explained with the help of the vorticity contour shown in the background of streamlines in Fig. 7 (b). The right side region shows that the vorticity is minimum and negative, turning the fluid clockwise. The left side region of the draft tube plane shows the maximum vorticity, which pushes the fluid in a counter-clockwise direction. The vorticity is nearly zero in the central region, representing the stagnation zone.

Similarly, streamlines of mode 3 for BEP and PL conditions are presented in Figs 9(a) and 9(b), respectively. Mode 3 has 0.10% and 13.05% energy at BEP and PL, respectively. A similar pattern to mode 2 is observed at BEP, but the lower part has less dominant rotation in the reverse direction of runner rotation than mode 2. The vorticity contour shows the positive region, as shown in mode 2. It shows that the core length is reduced slightly compared to mode 2. At PL, the instabilities in the mean flow induce large eddies, which are intermittent in space and time and have unstable inertia. These unstable eddies break into smaller eddies and possess a large amount of turbulent kinetic energy

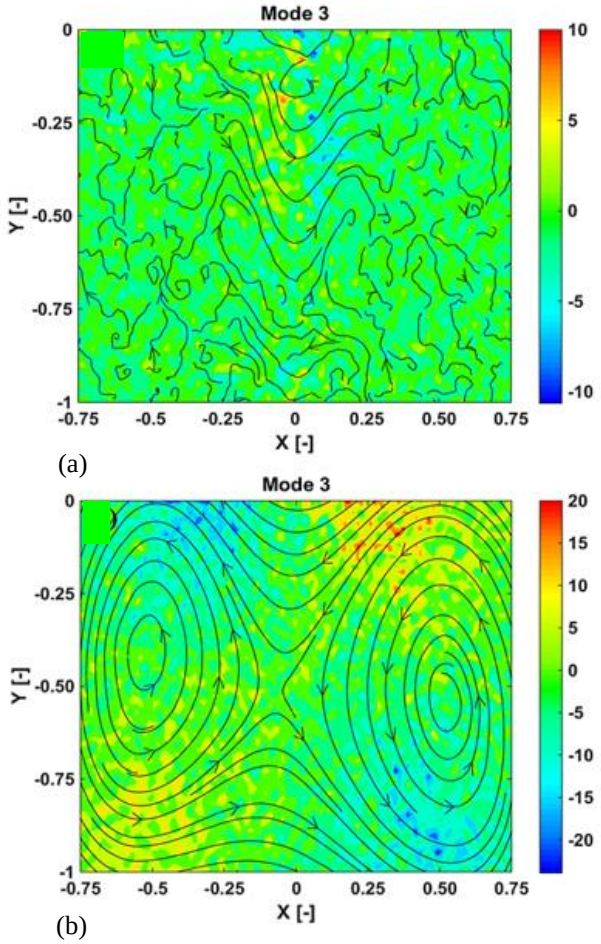

Fig. 9 (a) Vorticity contour with streamlines of mode 3 at BEP; (b) Vorticity contour with streamlines of mode 3 at PL

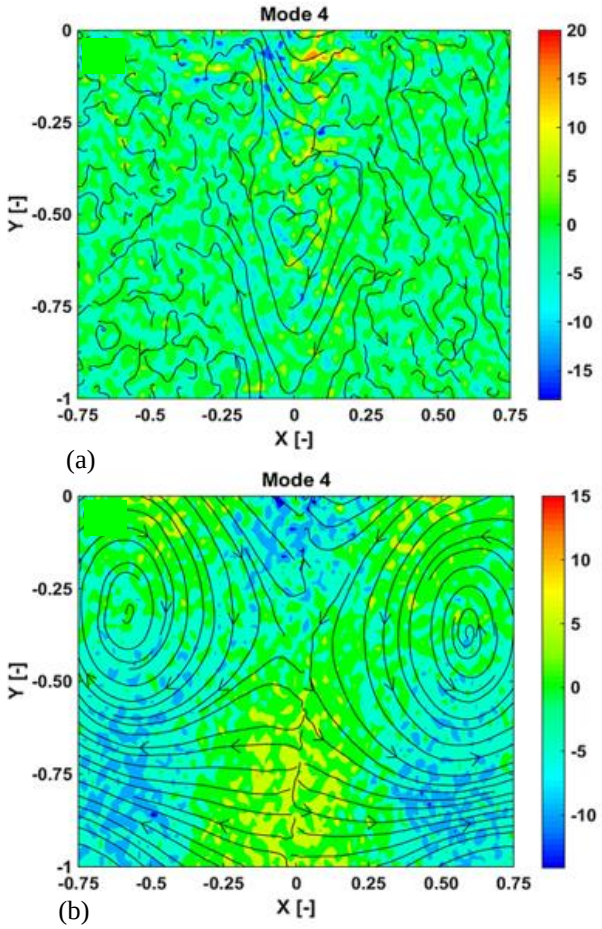

Fig. 10 (a) Vorticity contour with streamlines of mode 4 at BEP; (b) Vorticity contour with streamlines of mode 4 at PL

(TKE). Mode 3 at PL has two anticlockwise rotating eddies in pairs, which generally form due to the bursting of a large eddy (Hussain, 1986). This may be attributed to the release of the burst of TKE and the rapid diffusion of vorticity (Hamilton et al., 2017; Ali et al., 2018; Camp & Cal, 2019). The vorticity contours in Fig. 9 also show high positive and negative vorticity, making strong eddies. The negative and positive vorticity is present in diagonal directions, making the same direction of rotation for both eddies. The coherent structure's orientation looks like a giant vortex is being dissociated into two structures. With the high fluid velocity downstream of the runner, the high-velocity fluid moves towards the wall and pushes the low upward velocity flowing fluid towards the draft tube cone axis (Fig. 9b). This is similar to sweep and ejection phenomena occurring during the turbulent boundary layer bursting process. The flow reversal under the effect of APG and deceleration induces the axial velocity component around the stagnation region, which strongly promotes the burst phenomena (Hussain, 1986). Further, the circumferential component continuously decreases in the axial direction and induces the axial velocity component opposite the main flow direction. This component leads to a strong deceleration in the main flow when coupled with APG, as reported in the literature (Althaus et al., 1995; Kumar et al., 2021a).

Mode 4 at BEP condition is the last organizing structure, as the rest of the mode structures can be termed unorganized or incoherent. It is observed that the flow in mode 4 at BEP has a central rotating flow region opposite to the runner rotation direction, as shown in Fig. 10 (a), which was also observed earlier by Davidson (2015). The coherent structures at PL operating conditions are observed in up to eight modes. An analogous pattern can be observed in Fig. 10(b) and Fig. 11(a) of modes 4 and 5, respectively. Mode 4 in Fig. 10(b) and mode 5 in Fig. 11(a) are pair modes with almost similar energy contributions, around 2.76%, and 2.43%. These modes are inverted mirror images of each other. The negative vorticity is present in Figs 10(b) and 11(a), attracting low-energy fluids toward the draft tube wall. The positive vorticity in Figs 10(b) and 11(a) shows the fluid having high energy, replacing the low-energy fluid at the center of the draft tube. The positive vorticity in Fig. 12(b) shows a counter-clockwise rotation of the reverse flow zone. Mode 6 and mode 7 are also pair modes similar to mode 4 and mode 5; therefore, they are not shown here.

Mode 8, as shown in Fig. 11(b), shows the flow reversal at the center of the draft tube. Flow reversal forms a stagnation region due to the large APG and induced axial flow in the reverse direction. The flow reversal is also aligned with the runner's rotational direction.

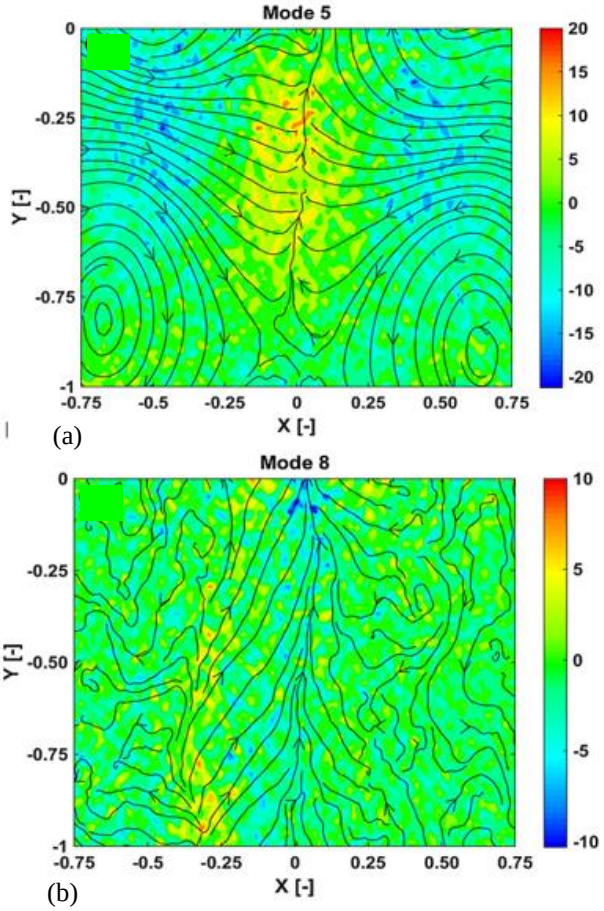

Fig. 11 (a) Vorticity contour with streamlines at PL (a) Mode 5; (b) Mode 8

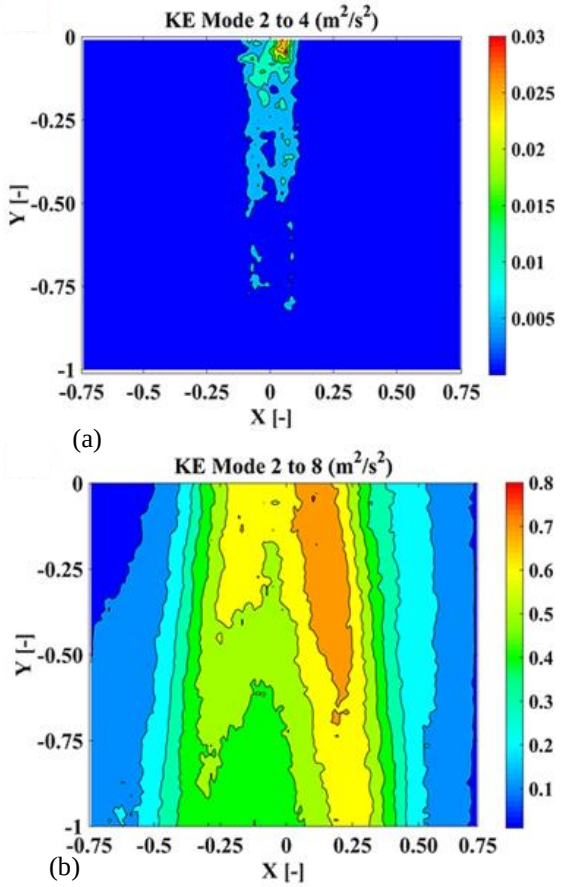

Fig. 12 KE of coherent modes (a) at BEP; (b) at PL (Kumar et al., 2021b)

The presence of flow reversal, generation of TKE through the bursting of coherent structure, eddies due to RVR, and structure of RVR give insight into the generation of flow instabilities in the flow field at PL condition. A counter-clockwise rotating central reverse flow zone (shown in Fig 11 (b)) and a clockwise rotating flow in Fig 8 (b) show counter-rotating and co-flowing vortex rope.

The kinetic energy contributions of these coherent and incoherent structures of various modes are discussed further. The KE of the first mode at BEP (see Fig. 6(b)) is around 99.21% and shows quasi-symmetry in KE distribution in the flow. The maximum kinetic energy is at the center of the draft tube cone, and the energy near the wall is much less. The percentage of the kinetic energy of the first mode at PL is a little more than half of BEP (around 50.72%), as shown in Fig. 5(b).

The contribution of coherent structure KE in the flow field at BEP and PL is shown in Figs. 12(a) and 12(b), respectively. The KE of a coherent structure for BEP is around 0.3% of the total KE, whereas, for PL, it is around 45.93%. The central region has the maximum energy because of the energy exchange between eddies formed in coherent structures. The magnitude of energy contribution of these coherent structures is less than that of mode 1. At BEP, only 0.3% of flow energy is associated with the flow instability generated as a vortex core. In contrast, at PL, around 45% of KE is associated with the secondary flow structures generated in the draft tube due to the presence of RVR, which generates the pressure pulsations, flow reversal, stagnation region, burst of coherent structures, formation and rolling of the shear layer, etc. Similarly, the contribution of incoherence is around 0.5% and 3.43% of the total KE for BEP and PL, respectively (see Fig. 13). The turbulence or incoherence is high for PL operating conditions due to the secondary flows in the draft tube cone.

3.2 Dissipation of Kinetic Energy

The energy equation of the flow in the draft tube of the Francis turbine is given by equation 2 as (Tennekes & Lumley, 1972).

$$\rho V_j \frac{\partial}{\partial x_j}(1/2 V_i V_i) = \frac{\partial}{\partial x_j}(\tau_{ij} V_i) - (\tau_{ij} S_{ij}) \quad (2)$$

where τ_{ij}, is the symmetric tensor, and 'S' is the local fluctuating strain tensor, and $\tau_{ij}\ S_{ij}$, is the deformation work. The dissipation energy of all modes is given by Equation 3

$$\varepsilon = 2\nu_a S : S \quad (3)$$

where ν_a is the viscosity of the flowing fluid. The strain tensor of the mth velocity vector field corresponds to mth decomposition and is given by equation 4 (Tennekes & Lumley, 1972; Davidson, 2015)

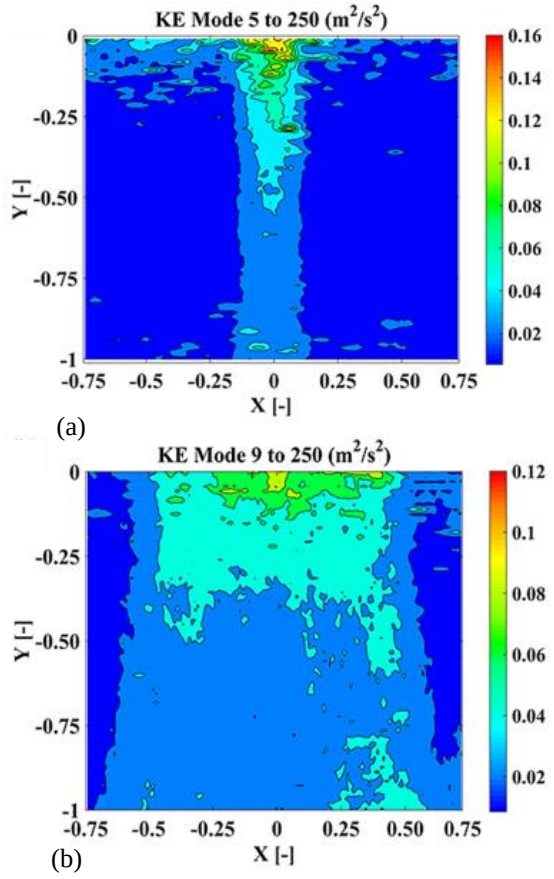

Fig. 13 (a) KE of incoherent modes at BEP; (b) KE of incoherent modes at PL (Kumar et al., 2021b)

$$S_{ij}^{m}=\frac{\alpha_i^m}{2}.\left(\frac{\partial \xi_i^m}{\partial x_j}+\frac{\partial \xi_j^m}{\partial x_i}\right) \tag{4}$$

The dissipation of TKE for the POD mode 1 at BEP and PL is shown in Fig. 14. The dissipation is around 4.19% and 2.57% of the kinetic energy present in mode 1 for BEP and PL. The dissipation rate is almost the same for the mean flow at both BEP and PL conditions. However, the dissipation region at BEP differs from that of PL in the draft tube. At BEP, maximum dissipation is present in the central region of the draft tube. An axis-symmetric vortex core is observed at the draft tube center, creating instability in the flow field.

For PL, the velocity gradients exist in the draft tube, so the dissipation occurs in the whole draft tube region (Goyal et al., 2017c). The maximum dissipation occurs in the region where the shear layer and fluctuating strain develop in the flow. At PL, the RVR is eccentrically rotating in the draft tube cone around the central stagnation region. The shear layer develops on the boundary of the stagnant region and around the RVR, where the maximum dissipation of energy occurs (Saarenrinne & Piirto, 2000; Ali et al., 2018). The Reynolds stresses were generated as a response of smaller eddies against the distortion imposed by the large eddies (Ali et al., 2017; Carbone & Bragg, 2020).

The KE dissipation of organized modes is shown in Fig. 15. For BEP, the contribution of organized motion is around 1.53%, and for PL, it is around 9.72% of the total

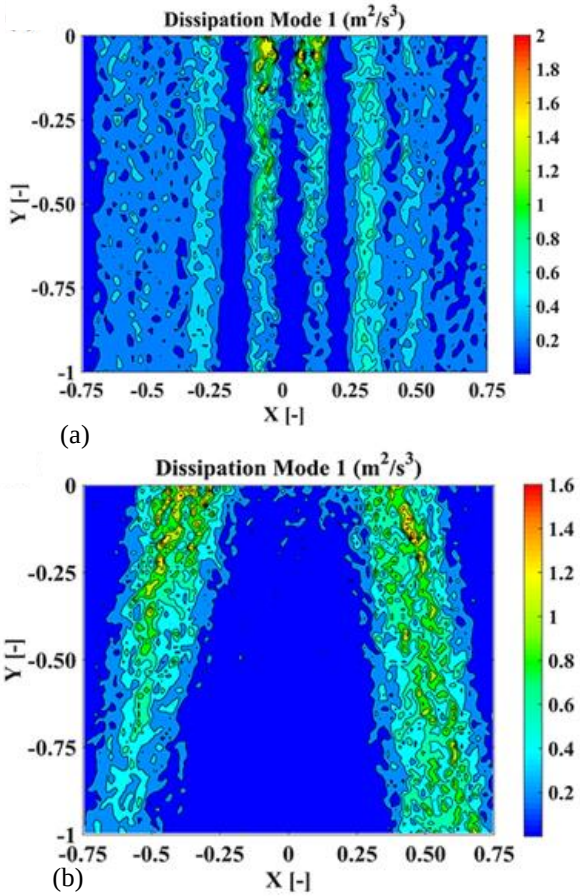

Fig. 14 Dissipation of TKE (m²/s³) of the first mode known as mean mode (a) BEP; (b) PL

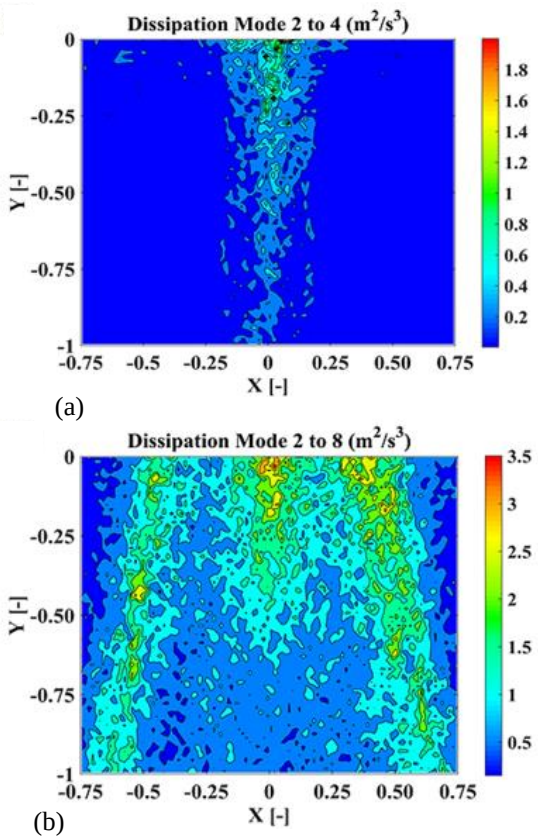

Fig. 15 Dissipation of TKE (m²/s³) of organized modes (a) BEP; (b) PL

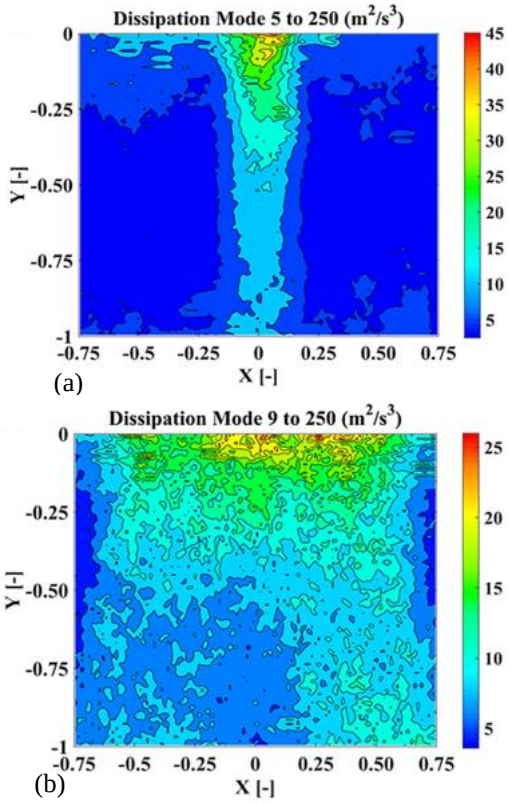

Fig. 16 (a) Dissipation of TKE (m^2/s^3) of unorganized modes at BEP (b) Dissipation of TKE (m^2/s^3) of unorganized modes at PL

KE. The dissipation at BEP is again limited to the central vortex core region, where the large eddies transfer their energy to the smaller eddies, further dissipating into heat. At PL, dissipation is present in nearly all regions. The organized modes, as shown above, show the turbulent bursts, formation of eddies, and shear layer in the whole draft tube. The bursting phenomenon of coherent structures and rapid diffusion of vortical structures play an important role in the transportation of TKE. The turbulent flow consists of coherent structures and phase-random (incoherent) motion (Hussain, 1986; Camp & Cal, 2019). The coherent structures are dynamic and rapidly changing via nonlinear interaction with other structures or decay via turbulent diffusion or incoherent turbulence.

The maximum dissipation through incoherent turbulence, as shown in Fig. 16 in both BEP and PL conditions. The maximum dissipation is 94.28% and 87.71% of the total KE at BEP and PL conditions. The energy conversion is maximum in the case of BEP, which means the pressure recovery in the draft tube is maximum, and the turbine's efficiency is maximum. Some of the KE is consumed at part load in forming secondary flow structures generated through flow instabilities. The stagnant region and RVR formation lead to a higher local fluctuating strain tensor, further developing the shear layer in the flow field. The energy conversion is less because of the formation of RVR in the draft tube, which leads to low-pressure recovery in the draft tube; hence, less turbine efficiency is obtained. Therefore, a methodology will be developed, like water injection or air injection in the center of the draft tube, which targets the stagnant zone and reduces or eliminates these organized structures, improving turbine efficiency.

3.3 Characteristic Turbulent Length Scales

The turbulent length scales measure the size of eddies in the turbulent flow. Two characteristic turbulent length scales are used to elucidate and measure the dissipation rate and distribution of the spatial turbulent kinetic energy. One is the Taylor macro-scale, usually imposed by the flow geometry, and the other one is Taylor micro scale for the inertial subrange eddies.

I. Taylor macro-scale (Λ)

It is generally related to shear-generated turbulence, which only depends on one length scale and one velocity scale. The macro scale is a function of the system's geometry and is given by equation 5, where k is the TKE, and ε is the dissipation rate. The KE due to large-scale turbulence is proportional to the square of the velocity. It is also called an integral scale of turbulence.

$$\Lambda = \frac{k^{3/2}}{\varepsilon} \tag{5}$$

Very little interaction occurs between the mean flow and fluctuating strain rate at high Reynolds numbers. To balance the turbulent energy production and its dissipation, Taylor microscale is introduced as below by equation 6.

$$\pi = \sqrt{\frac{10\nu k}{\varepsilon}} \tag{6}$$

At BEP, POD analysis shows an axis-symmetric vortex core in the draft tube center and finally dissipates the TKE in that region only. The Taylor scales at BEP are observed to be limited to this central region of the draft tube, whereas at PL condition, the length scales are present in the whole draft tube region. At PL condition, the RVR is precessing in the draft tube, and flow instabilities are present in the whole draft tube. Therefore, length scales are present in the whole draft tube region. Figure 17 shows the Taylor macro scale and its dissipation rate at BEP and PL. The eddies for both cases, which carry the energy, have a maximum length scale of around 600 mm near the upper side of the cone wall. This is almost double the size of the runner outlet diameter. The average size of macro eddies is around 89 mm and 180 mm (nearly half of the runner outlet diameter) at BEP and PL, respectively. Figure 18 shows that the turbulent micro length scale for BEP and PL varies between 1 to 5 mm, corresponding to the micro eddies in the TKE.

3.4 Phase Portraits

The phase portraits and amplitude plots of the first five modes are shown in Fig. 19 for PL conditions only. The phase portraits show the relation between two modes (like frequency, amplitude, and phase angle) from the flow field decomposition. Organized shapes are observed in these portraits; some look like an ellipse. Hydrodynamic coherent structures can be revealed when characteristic patterns, such as circles, ellipses, or Lissajous figures, appear in this plane. They can be associated with periodic

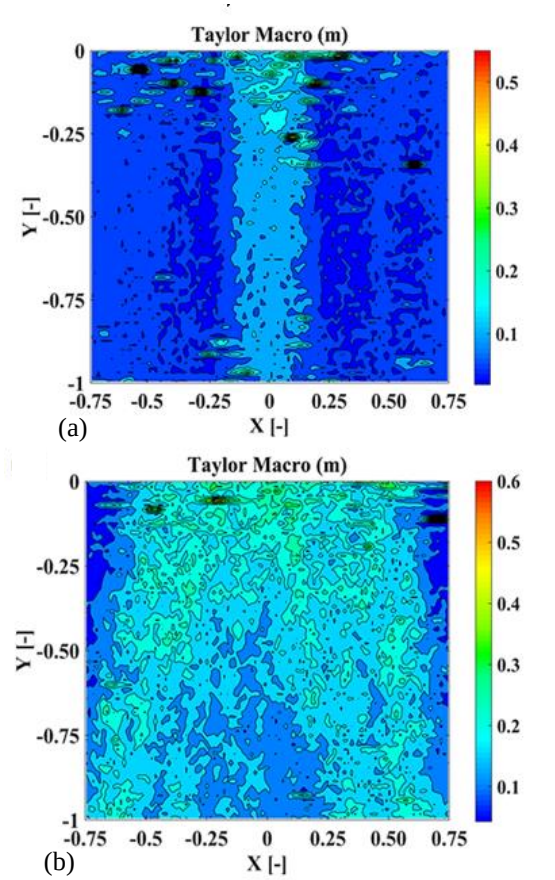

Fig. 17 (a) Taylor macro eddies at BEP; (b) Taylor macro eddies at PL

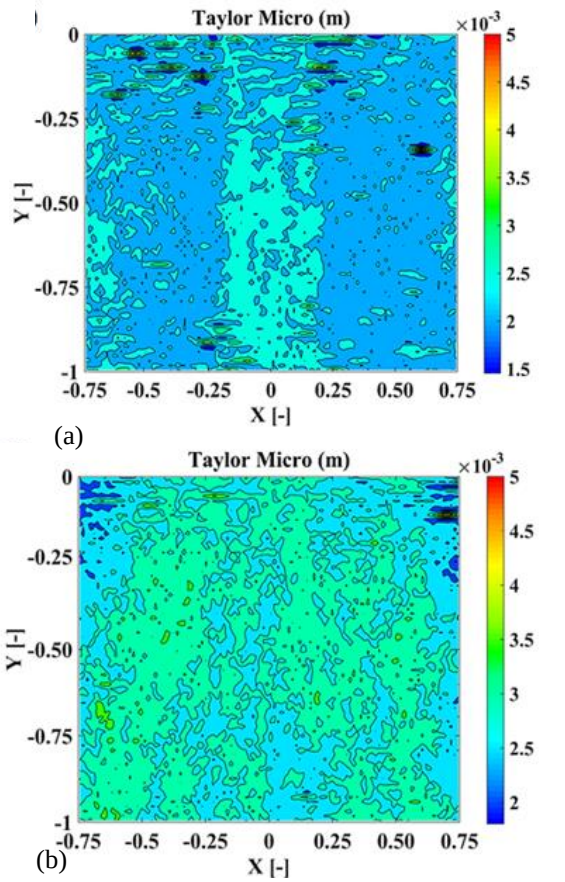

Fig. 18 (a) Taylor micro eddies at BEP; (b) Taylor micro eddies at PL

or intermittent structures like RVR in the draft tube at PL operating conditions. The temporal evolution of the phase portrait of the organized motion is given by equations (7-9) (Berkooz et al., 1993)

$$\overrightarrow{V_i^{(1,2)}}=\sqrt{2\lambda_G^{(1)}}\,\mathrm{Cos}\left(\varphi_i\right)\overrightarrow{\xi^{(1)}}+\sqrt{2\lambda_G^{(2)}}\,\mathrm{Sin}\left(\varphi_i\right)\overrightarrow{\xi^{(2)}} \tag{7}$$

$$\alpha_i^{(1)}\left(\varphi_i\right)=\sqrt{2\lambda_G^{(1)}}\,\mathrm{Cos}\left(\varphi_i\right) \tag{8}$$

$$\alpha_i^{(2)}\left(\varphi_i\right)=\sqrt{2\lambda_G^{(2)}}\,\mathrm{Sin}\left(\varphi_i\right) \tag{9}$$

where φ_i is the phase angle of ith mode, i = (1, 2, 3,…..m), and α_i has a similar dimension as of velocity (m/s).

The temporal coefficients of mode 1 and mode 2 are shown in Fig. 19(a), which can be related to the ellipse equation (equation 10) (Berkooz et al., 1993; Doulgerakis, 2010) derived from equations 8 and 9.

$$\frac{\alpha_i^{(1)2}}{2\lambda_G^{(1)}}+\frac{\alpha_i^{(2)2}}{2\lambda_G^{(2)}}=1 \tag{10}$$

The elliptical structure implies that the temporal coefficients of modes 1 and 2 have a phase difference of (π/4) in time. However, the amplitude variation of mode 2 is larger than mode 1, which shows a steep ellipsoidal shape in Fig. 19(a). The phase angle between the temporal coefficient of mode 2 and mode 3 is π/2 with different amplitudes. The phase portrait of modes 3 and 4 (Fig. 19 (c)) shows that two sine waves are orthogonally projected with a phase angle of π/4 and have a frequency twice the frequency of mode 2 and mode 3. A slowly rotating complex interaction of the traveling wave, with spanwise translating vortices having rapid phase changing phenomena, is observed through this portrait. This portrait shows (Fig. 19 (c)) that mode 4 has twice the pulsation as modes 2 and 3 and has a second harmonic RVR frequency. It also depicts that the vortical structure rotates with the same rotational frequency. It also shows from Fig. 19 (b-h) that the system alternates between fast travel and rest periods. This may confirm the RVR rotation in the draft tube cone. The modes 4 and 5 portraits show a perfect circular shape with a phase angle of π/2. In particular, circular shapes can suggest cyclic variations of modes related to vortices or coherent structures.

Figures 19 (b) and 19 (d) show the modal paring of periodic flow having symmetry in the flow vortices. Phase portraits of modes 2 and 3 (Fig. 19(b)) and modes 4 and 5 (Fig. 19 (d)) also represent the single oscillatory phenomena. When these spatial modes combine with their respective time coefficients, they produce an alternating and translating characteristic of vortices in the flow field. The phase portrait of modes 2 and 4 (Fig. 19 (e)) is the opposite of modes 2 and 3, with a phase angle of - π/4. Similarly, the phase portraits of modes 2 and 5 (Fig. 19(h)) with modes 3 and 5 (Fig. (19(f)) have a phase angle of π/2. The sinusoidal variation of the first five modes can be seen in Fig. 19 (i). The amplitude of mode 1 is higher than that of the other modes.

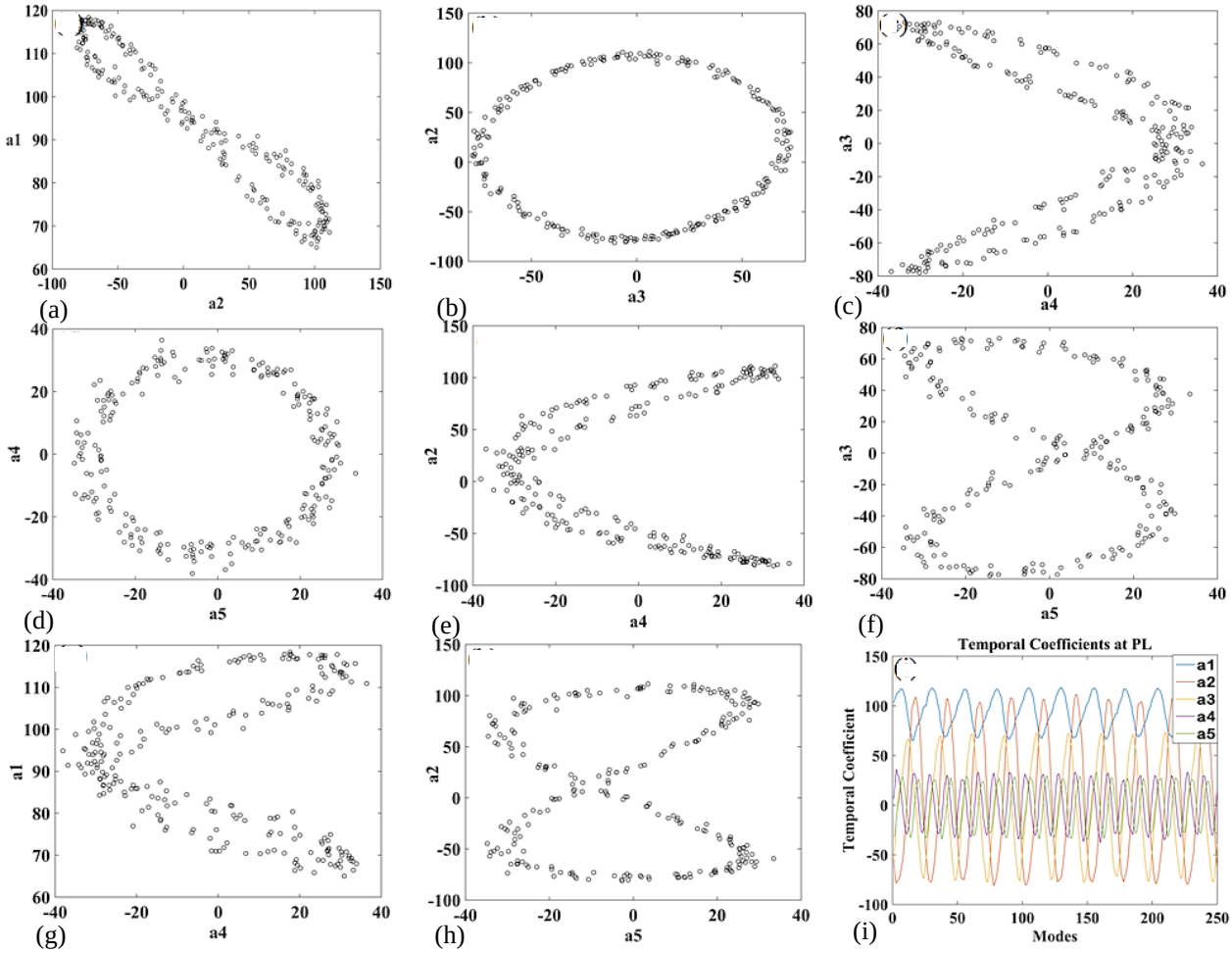

Fig. 19 Phase portrait (a)mode 1 and mode 2; (b) mode 2 and mode 3; (c) mode 3 and mode 4; (d) mode 4 and mode 5; (e) mode 2 and mode 4; (f) mode 3 and mode 5; (g mode 1 and mode 4; (h) mode 2 and mode 5; (i) Amplitute plot of temporal coefficients of mode 1 to mode 5.

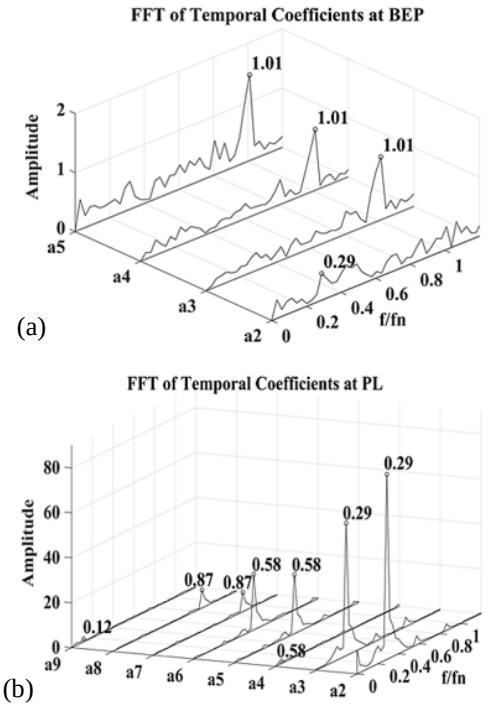

Fig. 20 (a) FFT of temporal coefficients of organized modes at BEP (b) FFT of temporal coefficients of organized modes at PL

The pressure pulsations in the draft tube due to the presence of RVR and its harmonic lead to very serious vibrations and machine failure situations. Therefore, the RVR and its harmonics amplitude have been carefully analyzed using FFT of the temporal coefficients as shown in Fig. 20. The curves are plotted for all coherent and first incoherent mode at BEP and PL operation. At BEP (Fig. 20 (a)), the frequencies about runner frequency were only observed for all modes except a_2. For a_2, the maximum amplitude was at 0.29, which may indicate the frequency of the axisymmetric rotating vortex core present at BEP. For PL operating condition Fig 20 (b), frequencies about the RVR (~0.29 f/f_n) and its harmonics (~0.58 and 0.87 f/f_n) showed maximum amplitudes at all the modes.

CONCLUDING REMARKS

Snapshot POD technique analyzes the flow field at a Francis turbine's two operating conditions: BEP and PL. Both conditions have different flow field structures. A vortex core is present in the flow field at BEP, whereas an RVR is observed at PL. The first mode is the mean mode and represents the mean flow structure of the flow field at both operating conditions. A counter-rotating and co-flowing vortex rope is observed via POD decomposition.

The TKE dissipation of organized modes at PL is nearly six times higher than that of the BEP condition. This generates secondary flow phenomena, which decreases the draft tube efficiency. The phase portrait shows the time evolution of these modes, showing the sinusoidal behavior harmonics of RVR. The FFT of temporal coefficients of POD modes at PL confirms the normalized RVR frequency of 0.29 and its harmonics. The FFT of BEP temporal coefficients shows the normalized frequency of 0.29 only at mode 2, which may be the axisymmetric rotating vortex core frequency. The amplitude of the vortex core at BEP is small compared to that of PL.

The vorticity, streamlined contours, and dissipation contours help the researchers to understand the flow field in detail and help target the zone in the flow field to mitigate these flow instabilities in the draft tube.

ACKNOWLEDGMENT

The authors acknowledge the experimental data of Dr. Rahul Goyal (see Goyal, 2017 (Goyal, 2017)) used in this work.

COMPLIANCE WITH ETHICAL STANDARDS:

Some parts of the paper were presented at the 30th IAHR Symposium on Hydraulic Machinery and Systems, a Conference paper entitled "Kumar, S., Khullar, S., Cervantes, M. J., & Gandhi, B. K. (2021b). Proper orthogonal decomposition of turbulent swirling flow of a draft tube at part load. IOP Conference Series: *Earth and Environmental Science*, *774*(1), 012091. https://doi.org/10.1088/1755-1315/774/1/012091"

Ethical approval: This article does not contain any studies with human participants or animals performed by any of the authors.

Informed consent: Not required.

DATA AVAILABILITY STATEMENT

The data that support the findings of this study are available with the corresponding author and can be shared on reasonable request.

CONFLICT OF INTEREST

The authors declare that they have no conflict of interest.

REFERENCES

Ali, N., Cortina, G., Hamilton, N., Calaf, M., & Cal, R. B. (2017). Turbulence characteristics of a thermally stratified wind turbine array boundary layer via proper orthogonal decomposition. *Journal of Fluid Mechanics*, *828*, 175–195. https://doi.org/10.1017/jfm.2017.492

Ali, N., Hamilton, N., DeLucia, D., & Bayoán Cal, R. (2018). Assessing spacing impact on coherent features in a wind turbine array boundary layer. *Wind Energy Science*, *3*(1), 43–56. https://doi.org/10.5194/wes-3-43-2018

Althaus, W., Brücker, C., & Weimer, M. (1995). Breakdown of Slender Vortices, *Fluid vortices*, 373–426). https://doi.org/10.1007/978-94-011-0249-0_9

Berkooz, G., Holmes, P., & Lumley, J. L. (1993). The proper orthogonal decomposition in the analysis of turbulent flows. *Annual Review of Fluid Mechanics*, *25*(1), 539–575. https://doi.org/10.1146/annurev.fl.25.010193.002543

Camp, E. H., & Cal, R. B. (2019). Low-dimensional representations and anisotropy of model rotor versus porous disk wind turbine arrays. *Physical Review Fluids*, *4*(2), 024610. https://doi.org/10.1103/PhysRevFluids.4.024610

Carbone, M., & Bragg, A. D. (2020). Is vortex stretching the main cause of the turbulent energy cascade? *Journal of Fluid Mechanics*, *883*, R2. https://doi.org/10.1017/jfm.2019.923

Davidson, P. A. (2015). *Turbulence: an introduction for scientists and engineers*. Oxford University Press.

Doulgerakis, Z. (2010). *Large scale vortex and strain dynamics in mixing vessels and implications for macro-mixing enhancement*. [Doctoral dissertation, University of London].

Goyal, R. (2017). *Flow field investigations on a Francis turbine model during steady and transient operations*. [Ph. D. thesis, Indian Institute of Technology], Roorkee.

Goyal, R., Cervantes, M. J., & Gandhi, B. K. (2017a). Vortex rope formation in a high head model Francis turbine. *Journal of Fluids Engineering*, *139*(4). https://doi.org/10.1115/1.4035224

Goyal, R., Cervantes, M. J., & Gandhi, B. K. (2017b). Characteristics of synchronous and asynchronous modes of fluctuations in Francis turbine draft tube during load variation. *International Journal of Fluid Machinery and Systems*, *10*(2), 164–175. https://doi.org/10.5293/IJFMS.2017.10.2.164

Goyal, R., Cervantes, M. J., Masoodi, F., & Sahu, P. (2023). A study of the velocity field during mitigation of vortex breakdown in model francis turbine at high load. *Journal of Fluids Engineering*, 1–42. https://doi.org/10.1115/1.4056614

Goyal, R., Gandhi, B. K., & Cervantes, M. J. (2017c). Experimental study of mitigation of a spiral vortex breakdown at high Reynolds number under an adverse pressure gradient. *Physics of Fluids*, *29*(10), 104104. https://doi.org/10.1063/1.4999123

Goyal, R., Gandhi, B. K., & Cervantes, M. J. (2018). PIV measurements in Francis turbine – A review and application to transient operations. *Renewable and*

Sustainable Energy Reviews, *81*, 2976–2991. https://doi.org/10.1016/j.rser.2017.06.108

Hamilton, N., Tutkun, M., & Cal, R. B. (2017). Anisotropic character of low-order turbulent flow descriptions through the proper orthogonal decomposition. *Physical Review Fluids*, *2*(1), 014601. https://doi.org/10.1103/PhysRevFluids.2.014601

Hussain, A. K. M. F. (1986). Coherent structures and turbulence. *Journal of Fluid Mechanics*, *173*, 303–356. https://doi.org/10.1017/S0022112086001192

Khozaei, M. H., Favrel, A., & Miyagawa, K. (2022). On the generation mechanisms of low-frequency synchronous pressure pulsations in a simplified draft-tube cone. *International Journal of Heat and Fluid Flow*, *93*, 108912. https://doi.org/10.1016/j.ijheatfluidflow.2021.108912

Kostas, J., Soria, J., & Chong, M. S. (2005). A comparison between snapshot POD analysis of PIV velocity and vorticity data. *Experiments in Fluids*, *38*(2), 146–160. https://doi.org/10.1007/s00348-004-0873-4

Kumar, S., Cervantes, M. J., & Gandhi, B. K. (2021a). Rotating vortex rope formation and mitigation in draft tube of hydro turbines – A review from experimental perspective. *Renewable and Sustainable Energy Reviews*, *136*, 110354. https://doi.org/10.1016/j.rser.2020.110354

Kumar, S., Khullar, S., Cervantes, M. J., & Gandhi, B. K. (2021b). *Proper orthogonal decomposition of turbulent swirling flow of a draft tube at part load*. IOP Conference Series: Earth and Environmental Science. https://doi.org/10.1088/1755-1315/774/1/012091

Kumar, S., Khullar, S., Goyal, R., Cervantes, M. J., & Gandhi, B. K. (2019). *POD analysis of turbulent swirling flow in draft tube of a high-head Francis turbine model at part load operation.* Proceedings of the 25th National and 3rd International ISHMT-ASTFE Heat and Mass Transfer Conference (IHMTC-2019). https://doi.org/10.1615/IHMTC-2019.1580

Liné, A. (2016). Eigenvalue spectrum versus energy density spectrum in a mixing tank. *Chemical Engineering Research and Design*, *108*, 13–22. https://doi.org/10.1016/j.cherd.2015.10.023

Liné, A., Gabelle, J. C., Morchain, J., Anne-Archard, D., & Augier, F. (2013). On POD analysis of PIV measurements applied to mixing in a stirred vessel with a shear thinning fluid. *Chemical Engineering Research and Design*, *91*(11), 2073–2083. https://doi.org/10.1016/j.cherd.2013.05.002

Litvinov, I., Sharaborin, D., Gorelikov, E., Dulin, V., Shtork, S., Alekseenko, S., & Oberleithner, K. (2022). Modal Decomposition of the Precessing Vortex Core in a Hydro Turbine Model. *Applied Sciences*, *12*(10), 5127. https://doi.org/10.3390/app12105127

Lumley, J. L. (1967). *The structure of inhomogeneous turbulence. in atmospheric turbulence and wave propagation.*

Lumley, J. L., & Meyer, R. E. (1981). *Transition and Turbulence*. Academic Press Inc, New York. https://doi.org/10.1016/B978-0-12-493240-1.50017-X

Podvin, B., & Fraigneau, Y. (2017). A few thoughts on proper orthogonal decomposition in turbulence. *Physics of Fluids*, *29*(2), 020709. https://doi.org/10.1063/1.4974330

Rudolf, P., & Jízdný, M. (2011). *Decomposition of the swirling flow fields.* Proceedings of the 4th IAHR International Meeting on Cavitation and Dynamic Problems in Hydraulic Machinery and Systems, 131–141.

Rudolf, P., & Štefan, D. (2012). *Decomposition of the swirling flow field downstream of Francis turbine runner.* IOP Conference Series: Earth and Environmental Science. https://doi.org/10.1088/1755-1315/15/6/062008

Rudolf, P., & Štefan, D. (2014). *Reduced order model of draft tube flow*. IOP Conference Series: Earth and Environmental Science,. https://doi.org/10.1088/1755-1315/22/2/022022

Rudolf, P., Urban, O., & Štefan, D. (2019). *Construction of a reduced-order dynamic model for prospective swirling flow control in hydraulic turbine draft tube.* IOP Conference Series: Earth and Environmental Science, 240, 022065. https://doi.org/10.1088/1755-1315/240/2/022065

Rudolf, P., Uruba, V., Štefan, D., & Hladík, O. (2013). *Analysis of the coherent vortical structures in a diffuser*. 5th International Workshop on Cavitation and Dynamic Problems in Hydraulic Machinery and Systems, Lausanne, Switzerland, 37.

Saarenrinne, P., & Piirto, M. (2000). Turbulent kinetic energy dissipation rate estimation from PIV velocity vector fields. *Experiments in Fluids*, *29*(7), S300–S307. https://doi.org/10.1007/s003480070032

Salehi, S., & Nilsson, H. (2022). Flow-induced pulsations in Francis turbines during startup - A consequence of an intermittent energy system. *Renewable Energy*, *188*, 1166–1183. https://doi.org/10.1016/j.renene.2022.01.111

Sarpkaya, T. (1971). On stationary and travelling vortex breakdowns. *Journal of Fluid Mechanics*, *45*(3), 545–559. https://doi.org/10.1017/S0022112071000181

Shahzer, M. A., Kim, S.-J., Cho, Y., & Kim, J.-H. (2022). Suppression of vortex rope formation and pressure fluctuation using anti-swirl fins in a Francis turbine model at part load condition with cavitation inception point. *Physics of Fluids*, *34*(9), 097106. https://doi.org/10.1063/5.0097685

Sirovich, L. (1987a). Turbulence and the dynamics of coherent structures. I. Coherent structures.

Quarterly of Applied Mathematics, *45*(3), 561–571. https://doi.org/10.1090/qam/910462

Sirovich, L. (1987b). Turbulence and the dynamics of coherent structures. II. Symmetries and transformations. *Quarterly of Applied Mathematics*, *45*(3), 573–582. https://doi.org/10.1090/qam/910463

Sirovich, L. (1987c). Turbulence and the dynamics of coherent structures. III. Dynamics and scaling. *Quarterly of Applied Mathematics*, *45*(3), 583–590. https://doi.org/10.1090/qam/910464

Stefan, D., & Rudolf, P. (2015). *Proper Orthogonal Decomposition of Pressure Fields in a Draft Tube Cone of the Francis (Tokke) Turbine Model*. Journal of Physics: Conference Series, 579, 012002. https://doi.org/10.1088/1742-6596/579/1/012002

Štefan, D., Rudolf, P., Muntean, S., & Susan-Resiga, R. (2017). Proper orthogonal decomposition of self-induced instabilities in decelerated swirling flows and their mitigation through axial water injection. *Journal of Fluids Engineering*, *139*(8). https://doi.org/10.1115/1.4036244

Tennekes, H., & Lumley, J. L. (1972). *A first course in turbulence*. MIT Press.

Tutkun, M., & George, W. K. (2017). Lumley decomposition of turbulent boundary layer at high Reynolds numbers. *Physics of Fluids*, *29*(2), 020707. https://doi.org/10.1063/1.4974746

Wang, L., Cui, J., Shu, L., Jiang, D., Xiang, C., Li, L., & Zhou, P. (2022). Research on the vortex rope control techniques in draft tube of francis turbines. *Energies*, *15*(24), 9280. https://doi.org/10.3390/en15249280